CRYSTAL GROWTH & DESIGN

Article

pubs.acs.org/crystal

Domain Matching Epitaxial Growth of In_2O_3 Thin Films on α-Al_2O_3(0001)

K. H. L. Zhang,[†] V. K. Lazarov,[‡] P. L. Galindo,[§] F. E. Oropeza,[†,#] D. J. Payne,[†,⊥] H. H.-C. Lai,[†] and R. G. Egdell*[,†]

[†]Department of Chemistry, University of Oxford, Inorganic Chemistry Laboratory, South Parks Road, Oxford OX1 3QR, United Kingdom

[‡]Department of Physics, University of York, Heslington, York, YO10 5DD, United Kingdom

[§]Departmento de Lenguajes y Sistemas Informáticos, CASEM, Universidad de Cádiz, Pol. Rio San Pedro s/n 11510, Puerto Real, Cadiz, Spain

ABSTRACT: Oxygen plasma assisted molecular beam epitaxy was used to grow thin films of In_2O_3 on α-Al_2O_3(0001) over a range of substrate temperatures between 300 and 750 °C. The crystal structures and morphologies were examined by X-ray diffraction, transmission electron microscopy, and atomic force microscopy. In all cases, the thermodynamically stable body-centered cubic phase *bcc*-In_2O_3 predominates in the films, with an epitaxial relationship $In_2O_3(111)\|Al_2O_3(0001)$ and In_2O_3 $[1\bar{1}10]\|Al_2O_3[10\bar{1}0]$ determined by matching between the sublattice oxygen atoms in Al_2O_3(0001) and the In atoms in In_2O_3(111): this involves a 30° rotation of the epilayer unit cell relative to that of the substrate and a 3:2 coincidence structure. A minority fraction of metastable rhombohedral *rh*-In_2O_3(0001) can be stabilized for substrate temperatures below 550 °C due to the similarity in the bonding symmetries between *rh*-In_2O_3 and α-Al_2O_3. Despite the large mismatches between In_2O_3 and Al_2O_3 for the two epitaxial systems discussed above (−13.2% for *bcc*-In_2O_3 and +15.1% for *rh*-In_2O_3), we show that the epitaxy can be maintained in both cases by matching small but different integral multiples of lattice planes of the In_2O_3 and the substrate at the interface between the two. Thus, the strain is effectively released by dislocations localized at the interface. This so-called domain matching epitaxial growth mode may open up a new route to fabrication of high-quality crystalline thin films of oxides on highly mismatched substrates.

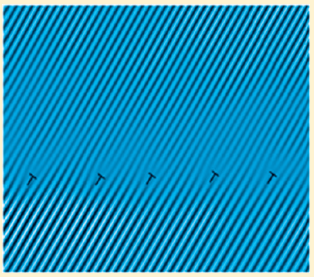

INTRODUCTION

Sn-doped In_2O_3 (widely but somewhat misleadingly known as indium tin oxide or ITO) combines optical transparency in the visible region with a high electrical conductivity. ITO is widely used as a transparent electrode material in photovoltaic devices, liquid crystal displays, and light emitting diodes, usually in the form of polycrystalline thin films deposited on glass or polymer substrates by sputtering technique.[1−3] There has however been a recent upsurge of interest in the epitaxial growth of single crystal thin films of In_2O_3.[4−6] This effort is motivated both by the need to access high-quality In_2O_3 thin films that exhibit intrinsic properties for detailed fundamental investigations[7−10] and by the potential use of high quality In_2O_3 thin films as the active layer in short wavelength optoelectronic devices.[11−13]

The phase of In_2O_3 thermodynamically stable under ambient conditions adopts the body-centered cubic (*bcc*) bixbyite structure, with space group $Ia\bar{3}$ and lattice parameter a = 10.1170 Å.[14] The structure may be regarded as a 2 × 2 × 2 superstructure of fluorite with ordered removal of O from 1/4 of the anion sites. Under high pressure conditions a rhombohedral (*rh*) phase is stabilized. The rhombohedral cell belongs to the $R3\bar{c}$ space group but can also be described in terms of a hexagonal cell with $a = b$ = 5.478 Å and c = 14.51 Å. There 6 formula units per hexagonal cell, and the volume per formula of 62.85 Å^3 for the *rh* phase is much smaller than the value of 64.72 Å^3 for the ambient *bcc* phase. The *rh* structure is based on a hexagonally close packed array of O ions with an occupation of 2/3 of the octahedral holes by In ions: this structure is also adopted by a number of other compounds with M_2O_3. Ball and stick representations of the two crystal structures are shown in Figure 1.

Cubic Y-stabilized ZrO_2 (YSZ) adopts the parent fluorite structure and provides an ideal substrate for growth of high quality thin films of *bcc*-In_2O_3 due to a small mismatch of only 1.7% between 2a for 17% Y-doped ZrO_2 and a for *bcc*-In_2O_3. Moreover the close relationship between the bixbyite and fluorite structures minimizes chemical mismatch at the interface between the two.[7,15−17] Thus In_2O_3 thin films with the highest reported electron mobilities of 226 cm^2 V^{-1} s^{-1} at room temperature and over 1200 cm^2 V^{-1} s^{-1} at 100 K have recently been grown on YSZ substrate by Bierwagen et al. using oxygen plasma assisted molecular beam epitaxy (OP-MBE).[18] Elsewhere it has been shown that atomically flat In_2O_3(111) films can be grown on YSZ(111) substrates — this surface has the lowest surface energy among the low index surfaces.[10,19−22] The availability of atomically flat films allowed investigation of the surface physics of In_2O_3 and revealed the presence of a pronounced electron accumulation layer arising from pinning

Received: November 9, 2011
Revised: December 15, 2011
Published: January 4, 2012

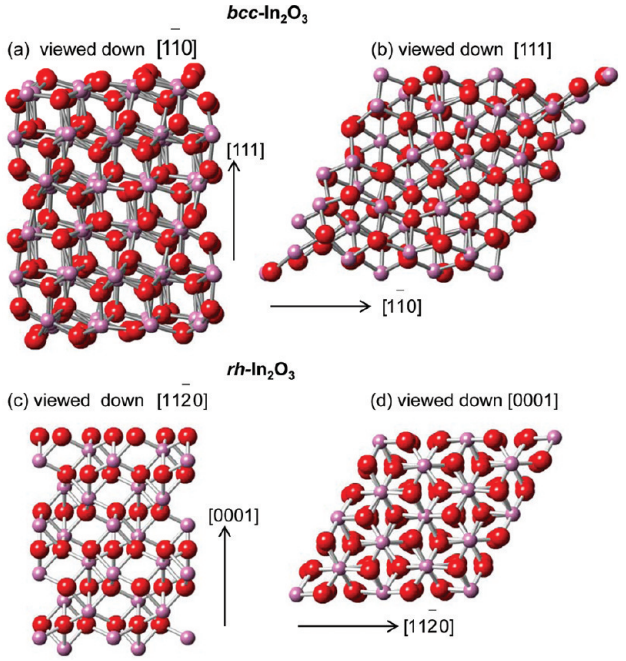

Figure 1. Ball and stick representations of crystal structures of *bcc*-In_2O_3 (a and b) and *rh*-In_2O_3 (c and d). In atoms are pale pink, and O atoms are dark red. The viewing directions and the in plane orientation are indicated in the figure.

of the Fermi level about 0.4 eV above the conduction band minimum.[10,23] However, the accumulation layer may be suppressed by oxygen plasma treatment, leading to flat band behavior.[24]

An alternative substrate to YSZ is α-Al_2O_3. This material is much cheaper than YSZ and is widely used for epitaxial growth of ZnO and GaN.[25−28] Like *rh*-In_2O_3, α-alumina or corundum belongs to the rhombohedral space group $R3\bar{c}$ and the structure is usually defined in terms of a hexagonal cell with $a = b = 4.759$ Å and $c = 12.991$ Å.[29] Chern et al. have used pulsed laser deposition to grow (111) oriented In_2O_3 films on *a*-plane (that is (11$\bar{2}$0) oriented) Al_2O_3.[30] Elsewhere Gao et al. used a vapor transport technique to grow (001) oriented nanowires on the same substrate.[31] In the current paper, we explore growth of In_2O_3 on the basal (0001) surface of Al_2O_3. Using the subscripts s and e to distinguish between the epilayer and the substrate, it can be seen that there is a close match between $3a_s = 14.277$ Å and $\sqrt{2}a_e = 14.308$ Å (which defines the (111) surface unit cell) for *bcc*-In_2O_3 since

$$m = (\sqrt{2}\,a_e - 3a_s)/3a_s = 0.00217$$

That is, the mismatch m defined in this way is only +0.217% (also +0.217% if the denominator is $\sqrt{2}a_e$). However, ionic positions within the unit cells do not coincide optimally when *bcc*-$In_2O_3[1\bar{1}0]\|Al_2O_3$ [11$\bar{2}$0]. Indeed Mei et al. found that an In_2O_3 epilayer grown on Al_2O_3(0001) by O-plasma MBE[32] at 680 °C was rotated by 30° so that *bcc*-$In_2O_3[1\bar{1}0]\|Al_2O_3$ [10$\bar{1}$0] with a mismatch m defined by a 2/3 coincidence structure:

$$m = (\sqrt{2}\,a_e - 2\sqrt{3}\,a_s)/2\sqrt{3}\,a_s = -0.132$$

It can be seen that $|m|$ now has a much bigger value with $m = -13.2\%$ (−15.2% with $\sqrt{2}a_e$ as the denominator). However, as will be discussed later, this orientation allows the hexagonal mesh of In ions to lie in reasonable registry with the O ions in the Al_2O_3 substrate. As with YSZ substrates, the epilayer is under tensile stress. A Hall mobility of 30 $cm^2\ V^{-1}\ s^{-1}$ for these films was somewhat disappointing.

Elsewhere Yang et al. have reported an in-plane epitaxial relationship *bcc*-$In_2O_3[1\bar{1}0]\|Al_2O_3$] [11$\bar{2}$0] for (111) oriented films grown by metallo-organic chemical vapor deposition (MOCVD) using $In(CH_3)_3$ and O_2 precursors at substrate temperatures between 550 and 750 °C.[33] This is a puzzling result because the [1$\bar{1}$0] direction is not orthogonal to [111]. The result is also at variance with the work of Ambacher and co-workers, who have made extensive studies of the growth of In_2O_3 on Al_2O_3(0001) by MOCVD using $In(CH_3)_3$ and H_2O as precursors.[34−39] At high flow rates of the $In(CH_3)_3$ precursor and at low substrate temperatures the *bcc* polymorph of In_2O_3 grows with (001) orientation, giving the out of plane epitaxial relationship *bcc*-$In_2O_3[001]\|Al_2O_3$ [0001].[34−38] This is a surprising result as the (001) surface of In_2O_3 is a polar Tasker type III surface[40] with a higher surface energy than the quadrupolar (111) surface.[17,19] In-plane, the films were found to be built up from square or rectangular domains rotated by 30° relative to each other[33] with *bcc*-$In_2O_3[1\bar{1}0]\|Al_2O_3$ [11$\bar{2}$0], etc. However, at higher temperatures and lower flow rates a biphasic mixture of *bcc*- and *rh*-In_2O_3 was obtained: phase pure *rh*-In_2O_3(0001) could be grown at 600 °C with very low $In(CH_3)_3$ flow rates of around 4 μmol/min.[34,36,39] Simple epitaxy with *rh*-$In_2O_3[0001]\|Al_2O_3$ [0001] and *rh*-$In_2O_3[10\bar{1}0]\|A1_2O_3$ [10$\bar{1}$0] was observed. This gives a mismatch:

$$m = (a_e - a_s)/a_s = +0.151$$

(The mismatch of +15.1% defined with a_s as the denominator decreases to +13.1% if defined with a_e as the denominator.) The *rh*-In_2O_3 epilayer is under pronounced compressive stress which may help account for stabilization of a phase that can be obtained in the bulk only at very high pressures.[41]

In this paper, we present an investigation into the epitaxial growth of *bcc*- and *rh*-In_2O_3 on α-Al_2O_3(0001) by OP-MBE. We show that despite the large mismatches between the epilayer and the substrate for both phases, it is possible to maintain epitaxial growth in both cases by matching different integral multiples of lattice planes of the In_2O_3 and the substrate.

EXPERIMENTAL SECTION

In_2O_3 films were grown on 1 cm × 1 cm α-Al_2O_3(0001) substrates in an ultrahigh vacuum oxide MBE system (SVT, USA) system with a base pressure of 5×10^{-9} mbar. This incorporated a hot lip indium effusion cell and a radio frequency (RF) oxygen plasma atom source operated at 200 W RF power with an oxygen background pressure of 3×10^{-5} mbar. Substrates were held by gravity in a recessed Mo mounting plate and heated radiatively using a graphite filament. The growth temperature was measured by a chromel-alumel thermocouple mounted immediately behind the substrate. This allows the temperature of the substrate to be set reproducibly within our own system, although we have no independent measurement of the temperature of the front face of the substrate during MBE growth. The Al_2O_3(0001) substrates were cleaned by exposure to the oxygen atom beam with a measured substrate temperature of 900 °C. Films were then grown over a range of substrate temperatures (T_s) between 300 and 750 °C in growth runs whose duration extended over a time of 3×10^3 s (50 min). The nominal growth rate was 0.035 nm s^{-1} calibrated using the thickness from high resolution transmission microscopy (HRTEM) measurements and atomic force microscopy (AFM) images.

High resolution X-ray diffraction (XRD) θ−2θ measurements were performed on a Philips Xpert diffractometer using monochromatic CuKα radiation (λ = 1.54060 Å). Specimens for cross-sectional

dx.doi.org/10.1021/cg201474h | Cryst. Growth Des. 2012, 12, 1000−1007

transmission electron microscopy (TEM) were prepared by cutting and mechanical grinding down to 5−10 μm, followed by thinning to electron transparency by Ar ion beam milling using a Gatan 691 Precision Ion Polishing System (PIPS). Cross-sectional TEM images were collected using a JEOL3000F microscope operating at 300 keV. The effect of epitaxial strain at the interface was analyzed using geometric phase analysis (GPA) of HRTEM images.[42] GPA strain measures were obtained after using a large area of the substrate as a reference. A Gaussian mask with standard deviation equal to 7.33 pixels was applied in Fourier space, corresponding to a spatial resolution of 0.43 nm. The axes were chosen along the principal directions of elastic symmetry, taking the x-axis parallel to the interface and the z-axis normal to the interface.

Optical absorption spectroscopy measurements were performed at room temperature on an ultraviolet−visible Varian Cary 5000 spectrometer.

RESULTS AND DISCUSSION

Overview of the Growth Morphology. The crystal structures of the In_2O_3 films grown at different temperatures were initially examined by simple $\theta-2\theta$ diffraction measurements. Typical XRD profiles are shown in Figure 2. It is clear

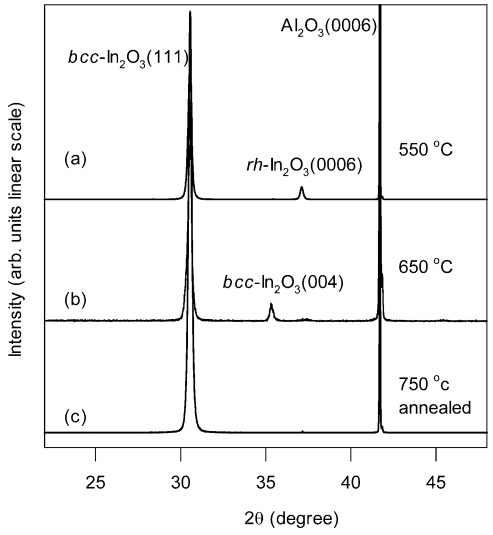

Figure 2. Wide scan $\theta-2\theta$ X-ray diffraction profile of In_2O_3 epilayer grown on α-Al_2O_3(0001) substrates at growth temperatures of (a) 450 °C, (b) 650 °C, (c) grown at 550 °C followed by annealing at 750 °C for 30 min.

that the thermodynamically stable bcc-In_2O_3 phase predominates in all films with the bcc-In_2O_3(111) plane parallel to the basal (0001) planes of the Al_2O_3 substrate. For films grown at T_s < 550 °C, a minority rh-In_2O_3 phase is also present with a signature provided by the (0006) peak located at 2θ = 30.57°. The rh-In_2O_3 phase was unstable against thermal treatment. As shown in Figure 1c, thermal annealing a film grown at T_s = 550 °C by heating at 750 °C for 30 min promotes the complete transformation of the minority rh-In_2O_3 phase into bcc-In_2O_3 to give single phase bcc-In_2O_3(111) thin films. Films grown at a substrate temperature higher than 650 °C only exhibit the stable bcc-In_2O_3 phase, with predominant bcc-(111) orientation but a small fraction of (001) oriented material.

AFM was used to examine the film morphology. Figure 3a shows large area AFM image (2000 nm × 2000 nm) of a film grown at 550 °C. The films are rough and granular with interconnected trigonal or hexgonal islands, reflecting the

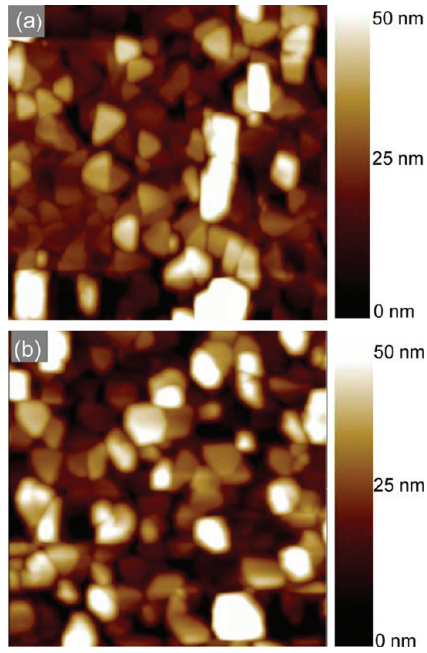

Figure 3. (a) 2000 nm × 2000 nm AFM image of In_2O_3 sample grown at 550 °C, (b) similar image after annealing at 750 °C for 30 min.

rotational symmetry of the substrate. The influence of the 3-fold symmetry is less obvious after post annealing a film grown at 550 at 750 °C.

Cross-sectional high resolution TEM was also used to examine the film morphology as well as the interfacial structure and epitaxial relationship between the In_2O_3 and Al_2O_3(0001). Figure 4a shows a low magnification image of a biphasic film

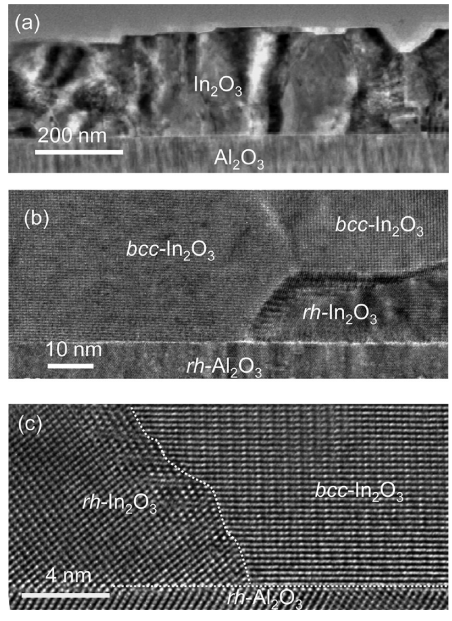

Figure 4. (a) Large area TEM image of In_2O_3 layer on Al_2O_3(0001) grown at 550 °C, (b) expanded image showing rh inclusion close to the interface surrounded by bcc-In_2O_3, (c) further expanded high resolution image showing contrasting structures of rh and bcc phases of In_2O_3.

grown at 550 °C viewed down the [1$\bar{2}$10] direction of the substrate. The film has a rough and irregular surface and several obvious boundaries between different domains: the roughness

dx.doi.org/10.1021/cg201474h | Cryst. Growth Des. 2012, 12, 1000−1007

inferred from both AFM and TEM is in fact greater than can be achieved in polycrystalline films prepared for example by spray pyrolysis.[43] Higher resolution images such as that shown in 4b in combination with selected area electron diffraction allowed us to establish that within the epilayer it was possible to distinguish between domains of the *bcc* and *rh* polymorphs of In_2O_3: the latter often appeared as inclusions within the *bcc* phase and usually confined to the interface. The meandering boundary between *bcc*-In_2O_3 and *rh*-In_2O_3 is identified in the higher resolution image of 4c which more clearly distinguishes between the two phases. For the *bcc* phase the epitaxial relationships are confirmed to be *bcc*-$In_2O_3[111]\|Al_2O_3$ [0001] and *bcc*-$In_2O_3[1\bar{1}0]\|Al_2O_3$ [10$\bar{1}$0]; that is, the [1$\bar{1}$0] direction of the unit cell for the In_2O_3 epilayer is rotated by 30° from the [11$\bar{2}$0] direction for the substrate, while for the *rh* phase as expected we have *rh*-$In_2O_3[0001]\|Al_2O_3$ [0001] and *rh*-$In_2O_3[10\bar{1}0]\|Al_2O_3$ [10$\bar{1}$0]; that is, the structure is unrotated.

Characterization of bcc-In_2O_3. As shown in Figure 1, the crystal structure of α-Al_2O_3 is based on a hexagonally close packed array of oxide ions with the close packed planes alternating in an ABABAB---- sequence. Between each pair of AB layers, 2/3 of the available octahedral holes are occupied by Al leaving 1/3 of the holes vacant. The Al ions do not occupy the centers of the holes but are displaced alternately up and down toward A and B layers, respectively. The positions of the empty sites rotate between the three available positions within successive layers, which coupled with the up/down displacements leads to a *c*-axis repeat containing six close packed O layers, that is, three AB bilayers. By contast in the bixbyite structure of In_2O_3, the In ions form an approximately cubic close packed array with 3/4 occupancy of the available tetrahedral holes by O.

An idealized view of the interfacial epitaxial relationship between Al_2O_3(0001) and *bcc*-In_2O_3(111) is shown in Figure 5. This schematic ignores the −13.2% mismatch discussed above and involves a 2/3 coincidence structure between the rotated surface unit cell for In_2O_3(111) and the substrate. The coordinate system for Al_2O_3 in this figure corresponds to that used by Lee and Lagerlof.[29] The separation between In atoms in the close packed (111) planes of In_2O_3 is d_{In-In} $I = \sqrt{2}a_e/4 = 3.577$ Å, while the separation between O atoms is the close packed planes of Al_2O_3(0001) is $d_{O-O} = a_s/\sqrt{3} = 2.748$ Å. The mismatch between these distances is given by

$$m = (d_{In-In} - d_{O-O})/d_{O-O} = +0.302$$

whereas for a 2/3 coincidence structure we have a smaller mismatch defined by

$$m = (2d_{In-In} - 3d_{O-O})/3d_{O-O} = -0.132$$

Within the idealized coincidence structure depicted in Figure 5, 1/4 of the In ions sit on top of O atoms in the basal close packed plane of alumina(0001), while the other In ions occupy 2-fold bridging sites. Alternatively, and more likely, it is shown in Figure 5 that by shifting the origin of epilayer cell, 1/4 of the In atoms can be brought into 3-fold hollow sites, although it is then impossible to avoid some of the In ions sitting above a subsurface Al atom. Note that the structure shown in Figure 5 differs from that proposed by Mei et al.[31] whose schematic structure erroneously suggested that $d_{In-In} \approx d_{O-O}$.

Figure 6a shows a higher resolution image of a *bcc*-In_2O_3 film viewed down the [11$\bar{2}$] direction of the In_2O_3 epilayer, corresponding to the [1$\bar{2}$10] direction of the substrate. The atomic structure and interplanar separations in the epilayer are

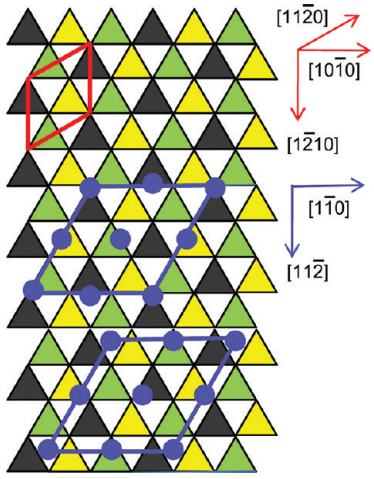

Figure 5. Schematic representation of epitaxial relationship between Al_2O_3(0001) and In_2O_3(111). The points of intersection of the mesh of triangle represent oxygen positions in the basal plane of Al_2O_3. The shaded triangles indicate that an octahedral hole lies under the triangle and the three colors of shading distinguish between octahedral holes that are (i) occupied by an upwardly displaced Al ion (ii) occupied by a downwardly displaced Al ion and (iii) empty. The hexagonal surface unit cell of alumina is shown in the top left-hand corner with the directions in a hexagonal coordinate system to the right (both red online). The In positions in 1/4 of an idealized $\sqrt{2}a_e \times \sqrt{2}a_e$ cell of In_2O_3(111) commensurate with the substrate are shown as closed circles (blue) in the lower part of the figure with the $\sqrt{2}/2a_e \times \sqrt{2}/2a_e$ cell highlighted (blue). The directions for this cell in a cubic coordinate system are shown to the right (blue). Two different cell origins are shown with the corners of the cell defined by on-top positions and 3-fold hollow site positions, respectively.

consistent with the bixbyite structure of In_2O_3 with spacings of 0.72 and 0.29 nm that are close to $a_e/\sqrt{2}$ and $a_e/2\sqrt{3}$ respectively. Further expanded images of the epilayer and substrate are shown in 6b and 6c. This pair of images confirms the near 2/3 coincidence in atomic spacings parallel to the substrate surface along the [10$\bar{1}$0] direction of the substrate and also confirms that the coincidence structure leaves residual tensile strain in the epilayer.

As mentioned above there is a mismatch of −13.2% between $\sqrt{2}a_e$ and $2\sqrt{3}a_s$. With misfits of less than 7−8% thin films can grow pseudomorphically with simple lattice matching epitaxy up to a critical thickness, beyond which it becomes energetically favorable to generate dislocations which release the strain induced by the substrate.[44−46] The smaller the lattice mismatch, the thicker the layer within which coherent strained epitaxy can be maintained. However for very large mismatches, as in the current study, so-called domain matching epitaxy is favored. Here different integral multiples of lattice planes containing densely packed rows are matched across the interface with introduction of periodic misfit dislocations. Figure 6d shows a Fourier-filtered image of the interface region using the [2$\bar{2}$04] and [6$\bar{2}$2] diffraction features from the substrate and epilayer respectively to reconstruct the real-space image. Quasi-periodic dislocations can be seen at the interface, with every 7 or 8 planes of In_2O_3(1$\bar{1}$0) matching with 6 or 7 planes of Al_2O_3(10$\bar{1}$0). Taking the 8 × d{In_2O_3(1$\bar{1}$0)} and 7 × d{Al_2O_3(10$\bar{1}$0)} domain matching structure we have a residual mismatch defined by

$$m = (8 \times \sqrt{2}\,a_e - 7 \times 2\sqrt{3}\,a_s)/7 \times 2\sqrt{3}\,a_s = -0.0081$$

dx.doi.org/10.1021/cg201474h | *Cryst. Growth Des.* 2012, 12, 1000−1007

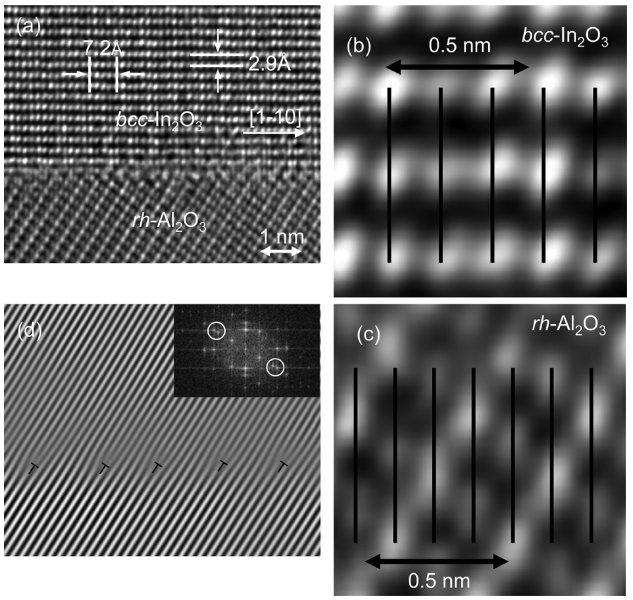

Figure 6. (a) High resolution TEM image of the interface region of *bcc*-In_2O_3 on $Al_2O_3(0001)$ viewed down the $[1\bar{2}10]$ direction of Al_2O_3. (b) Expanded view of part of the image of the epilayer. (c) Expanded view of part of the image of the substrate. The vertical lines in (b) and (c) identify atomic rows. Comparison between (b) and (c) shows that the total distance associated with four atomic rows in the epilayer is somewhat smaller than that associated with six atomic rows in the substrate, so that the 2/3 coincience structure discussed in the text places the epilayer under tensile stress. (d) Fourier filtered image using the $[2\bar{2}04]$ and $[6\bar{2}2]$ diffraction features from the substrate and epilayer respectively to reconstruct the real-space image of the interface. Periodic misfit dislocations localized at the interface are evident. The inset shows the diffraction pattern taken across the interface, with the region used for Fourier filtering highlighted.

while for $7 \times d\{In_2O_3(1\bar{1}0)$ and $6 \times d\{Al_2O_3(10\bar{1}0)$ we have

$$m = (7 \times \sqrt{2}\,a_e - 6 \times 2\sqrt{3}\,a_s)/6 \times 2\sqrt{3}\,a_s$$
$$= +0.0215$$

(the mismatches with $8 \times \sqrt{2}a_e$ or $7\sqrt{2}a_e$ in the denominator are respectively −0.82% and +0.212%). In principle, the 8/7 domain matching structure effectively accommodates the −13.2% mismatch by the introduction of periodic dislocations localized at the interface leaving a residual −0.8% tensile strain in the In_2O_3 films. Introduction of some regions with a 7/6 matching can lead to complete release of the mismatch. It is clear from the Fourier filtered image that dislocations are almost entirely confined to the interface region.

Accommodation of mismatch by periodic dislocations in domain matching epitaxy contrasts with layer matching epitaxy where pseudomorphic growth is followed by a strain relaxation process giving rise to formation of a high density of threading dislocations. These dislocations can act as scattering center for free electrons, degrading the transport properties of the thin films. In contrast, despite of the large mismatch between $In_2O_3(111)$ and $Al_2O_3(0001)$, mismatch accommodation by domain matching epitaxy can result in periodic dislocations localized at interface as soon as the material nucleates on the substrate, leaving the film on top of the interface nearly free of threading dislocation. Therefore domain matching epitaxy in systems with a large mismatch may open up new routes to fabrication of high-quality crystalline thin films.

To explore this idea, the distribution of strain at the interface between $Al_2O_3(0001)$ and $In_2O_3(111)$ was further characterized by geometric phase analysis of HRTEM images. Figure 7a shows a large area real space HRTEM image, while 7b shows a strain map for ε_{yy}, that is, for atomic separations normal to the interface. Here reference vectors are taken independently and separately for the substrate and the epilayer well away from the interface.

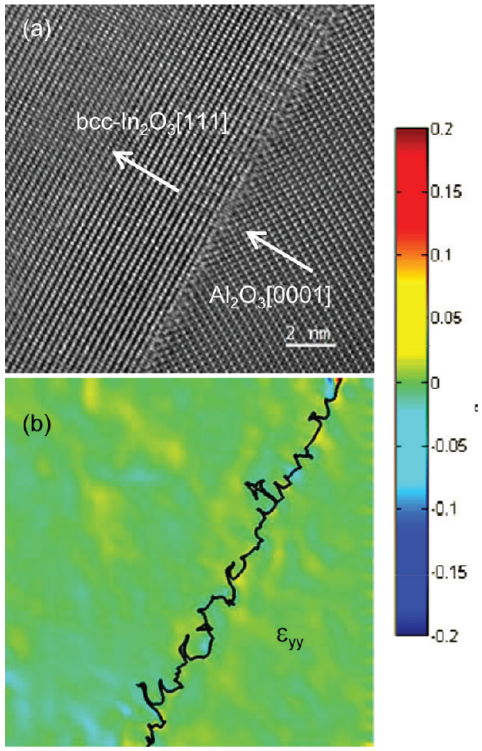

Figure 7. (a) Large area atomically resolved HRTEM image of interface between $Al_2O_3(0001)$ and *bcc*-$In_2O_3(111)$, (b) interface strain map showing ε_{yy} component (normal to surface) as derived from geometric phase analysis. See text for discussion of the color scale used in this map and explanation of the black line.

Two strain maps were then calculated using the two different reference vectors. Strain maps calculated using reference vectors for one material exhibit relatively small strain values within that material, but nonvalid strain values of a much higher absolute magnitude are obtained outside this area. Therefore, we have calculated the strain across the entire image using both reference vectors. In Figure 7b, the valid lower results are shown in a single image, with a black line used to delimit the areas referenced to the two different vectors. This line has been obtained by determining where the strain with respect to the substrate reference is equal to the strain with respect to the epilayer reference. The rugged shape of the line is due to the presence of the network of misfit dislocations. The displacements of atomic planes from the reference values are represented in terms of a chromatic scale where colors at the red end of the spectrum indicate an expansion of interplanar separations and colors at the blue end of the spectrum indicate a corresponding compression. An intermediate pale green color is associated with unchanged substrate separations. It is clear from the map that strain is localized close to the interface.

Characterization of *rh*-In_2O_3. Finally we turn to the minority *rh*-In_2O_3 phase found in some of the films. Figure 8a shows a HRTEM image of the interface between *rh*-In_2O_3 and $Al_2O_3(0001)$. As expected, simple epitaxial relationships *rh*-

dx.doi.org/10.1021/cg201474h | *Cryst. Growth Des.* 2012, 12, 1000−1007

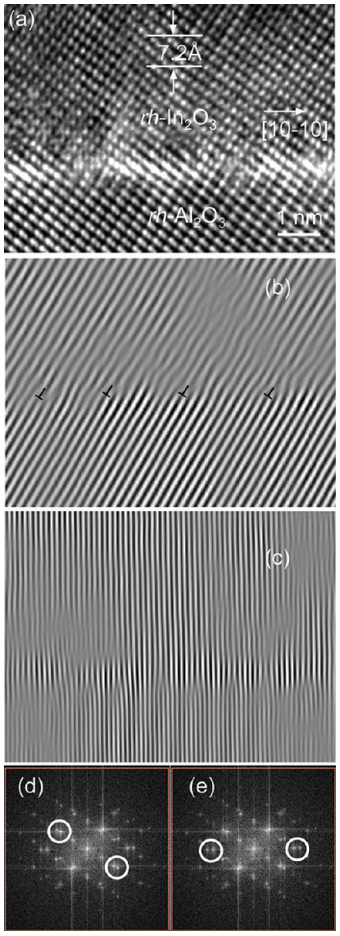

Figure 8. (a) High resolution TEM image of the interface region of *rh*-In_2O_3 on $Al_2O_3(0001)$ viewed down to $[1\bar{2}10]$ direction of Al_2O_3, showing the *rh*-on-*rh* epitaxial relationship (b) Fourier filtered image using the $[22\bar{4}4]$ diffraction features from the substrate and epilayer respectively to reconstruct the real-space image of the interface. Periodic misfit dislocations localised at the interface are highlighted. (c) Fourier filtered image using the $[33\bar{6}0]$ diffraction features from the substrate and epilayer respectively to reconstruct the real-space image of the interface. (d) and (e) show diffraction patterns taken across the interface with the regions used to reconstruct the images in (b) and (c) highlighted.

$In_2O_3[0001]\|Al_2O_3[0001]$ and *rh*-$In_2O_3[10\bar{1}0]\|Al_2O_3[10\bar{1}0]$ are found. As mentioned previously, in this system the in-plane mismatch is +15.1%, that is, the epilayer is not under compressive stress. In a fashion similar to that found for the *bcc* phase, this large mismatch can be accommodated by domain matching epitaxy involving $6 \times a_e[10\bar{1}0]$ and $6 \times a_s[10\bar{1}0]$, which leads to

$$m = (6 \times a_e - 7 \times a_s)/7 \times a_s = -0.0134$$

That is, the residual mismatch is only 1.34% (or 1.35% if defined with $6 \times a_e$ in the denominator).

Fourier filtered images using either $[22\bar{4}4]$ or $[33\bar{6}0]$ diffraction features to reconstruct the real space image are shown in Figure 8b,c. These images confirms that again there are a series of periodic misfit dislocations analogous to those shown in Figure 6d. However in this case dislocations and strain propagate further into the epilayer away from the interface. The large area HRTEM image and strain map corresponding to Figure 8 are shown in Figure 9. Again it can be seen that strain in the epilayer is mainly

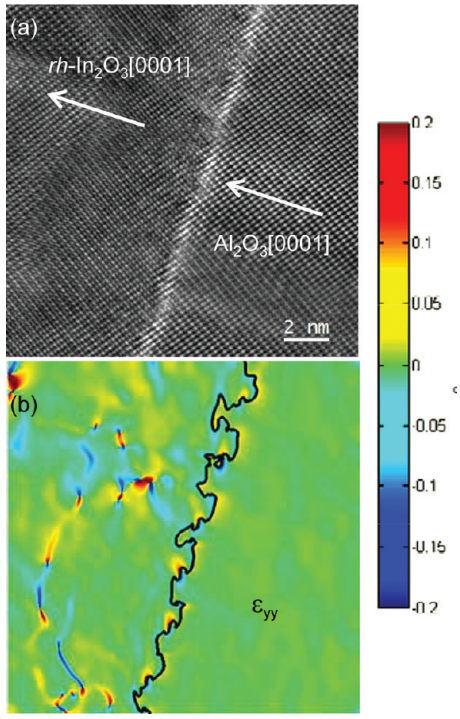

Figure 9. (a) Large area atomically resolved HRTEM image of interface between $Al_2O_3(0001)$ and *rh*-$In_2O_3(111)$, (b) interface strain map showing ε_{yy} component (normal to surface) as derived from geometric phase analysis.

confined to the interface region, although a crescent of alternating compressive and tensile strain is apparent in the lower part of the epilayer. It thus appears that misfit dislocations are less effective at confining strain to the interfacial region when the epilayer is under compressive stress.

The stabilization of metastable phases by growth of thin films on substrates with a matched crystal structure and lattice parameter is a well-known phenomenon, providing a valuable tool for synthesis of new thin film oxide materials not easily accessible by other techniques. Epitaxial stabilization is based on the favorable free-energy associated with structural coherence at the film/substrate interface.[47] In present case the metastable *rh*-In_2O_3 is stabilized due to the identical space groups of the epilayer and substrate. Moreover the substrate places the epilayer under compressive stress, thus promoting formation of the high pressure *rh* phase.

Optical Absorption Spectra. Figure 10 shows optical absorption spectra of for In_2O_3 films deposited at 450 °C and at 550 °C, followed by annealing at 750 °C. For the pure *bcc*-In_2O_3 film obtained after annealing at 750 °C significant the main absorption onset can be observed at around 3.6 eV, with a weaker low energy absorption tail extending down to below 3.0 eV. These spectra are consistent with previous optical measurements for *bcc*-In_2O_3.[23,48] It is now known that bcc-In_2O_3 has a direct but dipole forbidden bandgap of around 2.9 eV,[5,8,49] with the onset of dipole allowed transitions at about 0.8 eV higher energy. Thus the weak onset corresponds to the dipole forbidden gap and the strong onset to allowed transitions. For the sample grown at 450 °C, the relatively stronger low energy absorption around 3.4 eV not 3.0 eV results from the small fraction of *rh*-In_2O_3 phase stabilized at the interface region. As has been discussed in detail elsewhere,[49] the lower symmetry of the *rh* phase does not result in dipole forbidden transitions at the band edge so that there is stronger

dx.doi.org/10.1021/cg201474h | *Cryst. Growth Des.* 2012, 12, 1000−1007

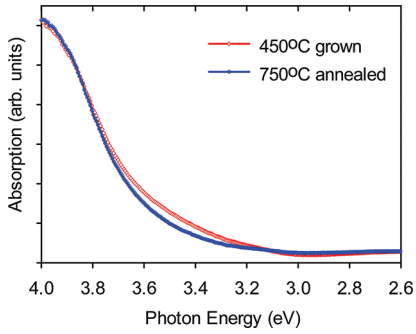

Figure 10. Optical absorption coefficient against photon energy for In_2O_3 film grown at 450 °C (red) and film grown at 550 °C followed by annealing at 750 °C for 30 min (blue).

absorption around 3 eV even though the bandgap of the *rh* phase is estimated to be about 0.1 eV bigger than for the bcc phase.[36]

CONCLUSIONS

In summary, we have shown both *bcc*- and *rh*-In_2O_3 can be grown epitaxially $Al_2O_3(0001)$ despite very different lattice parameters by matching different integral multiples of lattice planes of In_2O_3 with those of Al_2O_3. Residual strain is released by periodic misfit dislocation localized at in the interface. The growth of thermodynamically stable *bcc*-$In_2O_3(111)$ phase involves a 2/3 coincidence structure where the unit cell in the epilayer is rotated by 30° from the unit cell of the Al_2O_3. This allows In ions to come into coincidence with high symmetry sites of the close packed basal O layer of $Al_2O_3(0001)$, giving rise to an epitaxial relationships of $In_2O_3(111)\|Al_2O_3(0001)$ and $In_2O_3[1\bar{1}0]\|Al_2O_3[10\bar{1}0]$. Further work is however needed to establish whether In ions have a preference for 3-fold hollow sites or bridging and on-top sites. The similarity in the bonding symmetry between *rh*-In_2O_3 and *rh*-Al_2O_3 allows the stabilization of a metastable *rh*-$In_2O_3(0001)$ phase with a simple *rh*-on-*rh* configuration during low temperature growth. The epitaxial stabilization of the high pressure *rh* phase observed may also be promoted by the fact that *rh*-$Al_2O_3(0001)$ places *rh*-$In_2O_3(0001)$ under compressive stress. Domain matching epitaxy during growth of oxide layers on highly mismatched substrates offers exciting possibilities for fabrication of high quality thin films.

AUTHOR INFORMATION

Corresponding Author

*E-mail: russell.egdell@chem.ox.ac.uk.

Present Addresses

[#]Laboratory of Industrial Chemistry, Ruhr University Bochum, 44801 Bochum, Germany.

[⊥]Department of Materials, Imperial College London, Exhibition Road, London SW7 2AZ, UK.

ACKNOWLEDGMENTS

The Oxford MBE programme was supported by EPSRC Grant GR/S94148. K.H.L.Z. is grateful for support from the Oxford Clarendon Bursary Fund. D.J.P. acknowledges the support by the U.K. Royal Society Research Grant RG080399 and the award of a Junior Research Fellowship by Christ Church, University of Oxford. F.E.O. was supported by Pembroke College Oxford and FUNDAYACUCHO (Caracas, Venezuela).

REFERENCES

(1) Edwards, P. P.; Porch, A.; Jones, M. O.; Morgan, D. V.; Perks, R. M. *Dalton Trans.* **2004**, 2995.
(2) Granqvist, C. G. *Sol. Energy Mater. Sol. Cells* **2007**, *91*, 1529.
(3) Granqvist, C. G.; Hultaker, A. *Thin Solid Films* **2002**, *411*, 1.
(4) Koida, T.; Kondo, M. *J. Appl. Phys.* **2006**, *99*, 123703.
(5) Bourlange, A.; Payne, D. J.; Egdell, R. G.; Foord, J. S.; Edwards, P. P.; Jones, M. O.; Schertel, A.; Dobson, P. J.; Hutchison, J. L. *Appl. Phys. Lett.* **2008**, *92*, 092117.
(6) Bierwagen, O.; White, M. E.; Tsai, M. Y.; Speck, J. S. *Appl. Phys. Lett.* **2009**, *95*, 262105.
(7) Bourlange, A.; Payne, D. J.; Palgrave, R. G.; Zhang, H.; Foord, J. S.; Egdell, R. G.; Jacobs, R. M. J.; Veal, T. D.; King, P. D. C.; McConville, C. F. *J. Appl. Phys.* **2009**, *106*, 013703.
(8) Walsh, A.; Da Silva, J. L. F.; Wei, S. H.; Korber, C.; Klein, A.; Piper, L. F. J.; DeMasi, A.; Smith, K. E.; Panaccione, G.; Torelli, P.; Payne, D. J.; Bourlange, A.; Egdell, R. G. *Phys. Rev. Lett.* **2008**, *100*, 167402.
(9) King, P. D. C.; Veal, T. D.; Payne, D. J.; Bourlange, A.; Egdell, R. G.; McConville, C. F. *Phys. Rev. Lett.* **2008**, *101*, 116808.
(10) Zhang, K. H. L.; Payne, D. J.; Palgrave, R. G.; Lazarov, V. K.; Chen, W.; Wee, A. T. S.; McConville, C. F.; King, P. D. C.; Veal, T. D.; Panaccione, G.; Lacovig, P.; Egdell, R. G. *Chem. Mater.* **2009**, *21*, 4353.
(11) Hosono, H. *Thin Solid Films* **2007**, *515*, 6000.
(12) Nomura, K.; Ohta, H.; Ueda, K.; Kamiya, T.; Hirano, M.; Hosono, H. *Science* **2003**, *300*, 1269.
(13) Thomas, G. *Nature* **1997**, *389*, 907.
(14) Marezio, M. *Acta Crystallogr.* **1966**, *20*, 723.
(15) Morales, E. H.; Diebold, U. *Appl. Phys. Lett.* **2009**, *95*, 253105.
(16) Morales, E. H.; He, Y. B.; Vinnichenko, M.; Delley, B.; Diebold, U. *New J. Phys.* **2008**, *10*, 125030.
(17) Zhang, K. H. L.; Walsh, A.; Catlow, C. R. A.; Lazarov, V. K.; Egdell, R. G. *Nano Lett.* **2010**, *10*, 3740.
(18) Bierwagen, O.; Speck, J. S. *Appl. Phys. Lett.* **2010**, *97*, 072103.
(19) Walsh, A.; Catlow, C. R. A. *J. Mat. Chem.* **2010**, *20*, 10438.
(20) Walsh, A.; Catlow, C. R. A.; Zhang, K. H. L.; Egdell, R. G. *Phys. Rev. B* **2011**, *83*, 161202.
(21) Zhang, K. H. L.; Lazarov, V. K.; Veal, T. D.; Oropeza, F. E.; McConville, C. F.; Egdell, R. G.; Walsh, A. *J. Phys.: Condens. Matter* **2011**, *23*, 334211.
(22) Zhang, K. H. L.; Lazarov, V. K.; Lai, H. H. C.; Egdell, R. G. *J. Cryst. Growth* **2011**, *318*, 345.
(23) King, P. D. C.; Veal, T. D.; Fuchs, F.; Wang, C. Y.; Payne, D. J.; Bourlange, A.; Zhang, H.; Bell, G. R.; Cimalla, V.; Ambacher, O.; Egdell, R. G.; Bechstedt, F.; McConville, C. F. *Phys. Rev. B* **2009**, *79*, 205211.
(24) Chen, Y. F.; Bagnall, D. M.; Koh, H. J.; Park, K. T.; Hiraga, K.; Zhu, Z. Q.; Yao, T. *J. Appl. Phys.* **1998**, *84*, 3912.
(25) Bierwagen, O.; Speck, J. S.; Nagata, T.; Chikyow, T.; Yamashita, Y.; Yosikawa, H.; Kobyashi, K. *Appl. Phys. Lett.* **2011**, *98*, 172101.
(26) Chen, Y. F.; Ko, H. J.; Hong, S. K.; Yao, T. *Appl. Phys. Lett.* **2000**, *76*, 559.
(27) Strite, S.; Morkoc, H. *J. Vac. Sci. Technol. B* **1992**, *10*, 1237.
(28) Zhu, Q.; Botchkarev, A.; Kim, W.; Aktas, O.; Salvador, A.; Sverdlov, B.; Morkoc, H.; Tsen, S. C. Y.; Smith, D. J. *Appl. Phys. Lett.* **1996**, *68*, 1141.
(29) Lee, W. E.; Lagerlof, K. P. D *J. Electron Microsc. Tech.* **1985**, *2*, 247.
(30) Chern, M. Y.; Huang, Y. C.; Xu, W. L. *Thin Solid Films* **2007**, *515*, 7886.
(31) Gao, J.; Chen, R.; Li, D. H.; Jiang, L.; Ye, J. C.; Ma, X. C.; Che, X. D.; Xiong, Q. H.; sun, H. D.; Wu, T. *Nanotechnology* **2011**, *22*, 195706.
(32) Mei, Z. X.; Wang, Y.; Du, X. L.; Zeng, Z. Q.; Ying, M. J.; Zheng, H.; Jia, J. F.; Xue, Q. K.; Zhang, Z. *J. Cryst. Growth* **2006**, *289*, 686.
(33) Yang, F.; Ma, J.; Feng, X. J.; Kong, L. Y. *J. Cryst. Growth* **2008**, *310*, 4054.

(34) Wang, C. Y.; Cimalla, V.; Romanus, H.; Kups, T.; Ecke, G.; Stauden, T.; Ali, M.; Lebedev, V.; Pezoldt, J.; Ambacher, O. *Appl. Phys. Lett.* **2006**, *89*, 011904.
(35) Lozano, J. G.; Morales, F. M.; Garcia, R.; Gonzalez, D.; Lebedev, V.; Wang, C. Y.; Cimalla, V.; Ambacher, O. *Appl. Phys. Lett.* **2007**, *90*, 091901.
(36) Wang, C. Y.; Cimalla, V.; Romanus, H.; Kups, T.; Niebelschutz, M.; Ambacher, O. *Thin Solid Films* **2007**, *515*, 6611.
(37) Ali, M.; Wang, C. Y.; Roehlig, C. C.; Cimalla, V.; Stauden, T.; Ambacher, O. *Sens. Actuator B-Chem.* **2008**, *129*, 467.
(38) Wang, C. Y.; Cimalla, V.; Lebedev, V.; Kups, T.; Ecke, G.; Hauguth, S.; Ambacher, O.; Lozano, J. G.; Morales, F. M.; Gonzalez, D. *Physica Status Solidi C - Current Topics in Solid State Physics*; Palacios, T., Jena, D., Eds.; Wiley-VCH Verlag Gmbh: Weinheim, 2008; Vol. *5*, No. 6.
(39) Wang, C. Y.; Dai, Y.; Pezoldt, J.; Lu, B.; Kups, T.; Cimalla, V.; Ambacher, O. *Cryst. Growth Des.* **2008**, *8*, 1257.
(40) Tasker, P. W. *J. Physics C-Solid State Physics* **1979**, *12*, 4977.
(41) Shannon, R. D. *Solid State Commun.* **1966**, *4*, 629.
(42) Galindo, P. L.; Kret, S.; Sanchez, A. M.; Laval, J. Y.; Yanez, A.; Pizarro, J.; Guerrero, E.; Ben, T.; Molina, S. I. *Ultramicroscopy* **2007**, *107*, 1186.
(43) Korotcenkov, G.; Brinzari, V.; Cerneavschi, A.; Cornet, A.; Morante, J.; Cabot, A.; Arbiol, J. *Sensors & Actuators: B. Chemical* **2002**, *84*, 37.
(44) Narayan, J.; Larson, B. C. *J. Appl. Phys.* **2003**, *93*, 278.
(45) Grundmann, M.; Bontgen, T.; Lorenz, M. *Phys. Rev. Lett.* **2010**, *105*, 146102.
(46) Saint-Girons, G.; Cheng, J.; Regreny, P.; Largeau, L.; Patriarche, G.; Hollinger, G. *Phys. Rev. B* **2009**, *80*, 155308.
(47) Gorbenko, O. Y.; Samoilenkov, S. V.; Graboy, I. E.; Kaul, A. R. *Chem. Mater.* **2002**, *14*, 4026.
(48) Hamberg, I.; Granqvist, C. G.; Berggren, K. F.; Sernelius, B. E.; Engstrom, L. *Phys. Rev. B* **1984**, *30*, 3240.
(49) Fuchs, F.; Bechstedt, F. *Phys. Rev. B* **2008**, *77*, 155107.